

See discussions, stats, and author profiles for this publication at: <https://www.researchgate.net/publication/24011110>

# Primary Conformation Change in Bacteriorhodopsin on Photoexcitation

ARTICLE *in* BIOPHYSICAL JOURNAL · MARCH 2009

Impact Factor: 3.97 · DOI: 10.1016/j.bpj.2008.10.050 · Source: PubMed

---

CITATIONS

19

---

READS

19

2 AUTHORS, INCLUDING:



[Atsushi Yabushita](#)

National Chiao Tung University

74 PUBLICATIONS 282 CITATIONS

SEE PROFILE

# Primary Conformation Change in Bacteriorhodopsin on Photoexcitation

Atsushi Yabushita<sup>†‡\*</sup> and Takayoshi Kobayashi<sup>†‡§||</sup>

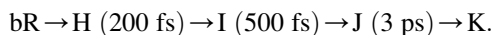
<sup>†</sup>Department of Electrophysics, National Chiao-Tung University, Hsinchu 300, Taiwan; <sup>‡</sup>Department of Physics, The University of Tokyo, Tokyo 113-0033, Japan; <sup>§</sup>JST, ICORP, Saitama 332-0012 Japan; <sup>¶</sup>Department of Applied Physics and Chemistry and Institute for Laser Science, University of Electro-Communications, Tokyo 182-8585, Japan; and <sup>||</sup>Institute of Laser Engineering, Osaka University, Osaka, 565-0971, Japan

**ABSTRACT** Ultrafast dynamics of bacteriorhodopsin (bR) has been extensively studied experimentally and theoretically. However, there are several contradictory results reported, indicating that its detailed dynamics and initial process have not yet been fully clarified. In this work, changes in the amplitude and phase of molecular vibration in the isomerization process of bR were real-time probed simultaneously at 128 different wavelengths through intensity modulation of the electronic transition. Systematic information on the transient change in continuous spectrum extending from 505 nm (2.45 eV) to 675 nm (1.84 eV) showed different dynamics in each spectral region reflecting the difference in the excited states and intermediates dominating the dynamics during the photoisomerization. Careful analysis of the transient spectral changes and spectrograms calculated from the vibrational real-time traces elucidated that the primary event just after photoexcitation is the deformation of the retinal configuration, which decays within 30 fs near the C=N bond in the protonated Schiff base. The intensity of C=N stretching mode starts to decrease before the initiation of the frequency modulation of the C=C stretching mode. The C=C stretching mode frequency was modulated by a coupled torsion around the C<sub>13</sub>=C<sub>14</sub> bond, leading to the photoisomerization around the bond. This study clarified the dynamics of the C=N and C=C stretching modes working as key vibration modes in the photoisomerization of bR. Furthermore, we have elucidated the modulation and decay dynamics of the C=C stretching mode in the photoreaction starting from H (Franck-Condon excited state) followed by I (twisted excited), and J (first intermediate) states.

## INTRODUCTION

Photoisomerization of rhodopsin is the primary key reaction in the vision process. However, the ultrafast time-resolved observation of the process is difficult because the rhodopsin does not recover after photobleaching *in vitro*. On the other hand, the membrane protein bacteriorhodopsin (bR) (1,2) extracted from bacteria is more stable than artificial chemicals and is a promising candidate for functional materials for optical memory and switch ((3), and see Stuart et al. (11)). The physiological function of bR in live bacteria is proton pumping to produce a chemical potential for ATP synthesis. This pump is optically triggered by the *trans-cis* photoisomerization, which is closely related to the *cis-trans* photoisomerization of rhodopsin in the vision process (4). Because of these interesting physiological and artificial functionalities, the primary process in bR has been thoroughly studied both theoretically (5,6) and experimentally (7–13).

The process is understood in the following way in most research articles (1):



However, there are still controversial experimental results reported. For example, Ruhman's group showed experimentally that locked retinal contained in bR exhibits similar photoinduced spectral change to that of ordinary bR (14,15).

Atkinson's group claimed that the long-believed isomerization process is not taking place in the primary process even

in the J intermediate (16). Meanwhile, the J intermediate is already often assigned as a ground-state species in which retinal is isomerized to a 13-*cis* configuration, as mentioned by Ruhman et al. (14). Furthermore, the problem of two theoretical models, i.e., a two-state, two-mode model and a three-state model of the photoisomerization proposed by the groups of Olivucci (5,17) and Schulten (6,18), respectively, has not yet been solved. Recent studies of the photoisomerization model of the retinyl chromophore show the dynamics after the photoexcitation (19,20); however, the details of the transient states are still contentious.

The reason the photoisomerization yield of bR is ~0.67 is explained as follows. The excited-state wave packet oscillates with a period of ~400 fs in the potential surface of the excited state. When it crosses the bottom of the potential surface toward the direction to form the J intermediate (or initial ground state), the excited population has a chance to cross the conical intersection into the J state (or initial ground state). This is why some transition of excited bR back to the initial ground state occurs. Clarification of these ultrafast dynamics needs direct observation of the transition state in the photoisomerization.

Unknown transient existence of intermediate species in the photoisomerization can be revealed by ultrafast laser experiments using ultrashort laser pulses, as are performed for the chemical reactions (21,22). The ultrafast spectroscopy is complementary to an x-ray diffraction method used by Anfinrud and co-workers (23) and electron diffraction methods developed by Miller and colleagues (24) and Zewail and colleagues (25). Instantaneous vibrational amplitude was detected with subfemtosecond resolution in

Submitted July 10, 2008, and accepted for publication October 15, 2008.

\*Correspondence: yab731@gmail.com

Editor: Shin'ichi Ishiwata.

© 2009 by the Biophysical Society  
0006-3495/09/02/1447/15 \$2.00

doi: 10.1016/j.bpj.2008.10.050

this study because the short pulse duration and high signal/noise ratio provide much higher time resolution than electron and x-ray diffraction experiments. Also, the method can be used for the measurements of amorphous and liquid-phase materials, to which x-ray or electron diffraction is difficult to apply. In our previous article (26), time-resolved absorbance change measurements elucidated ultrafast changes in frequencies of in-plane and out-of-plane bending modes associated with the structural change in real time during the photoisomerization including transition states. Femtosecond stimulated Raman spectroscopy with high time and spectral resolution was applied to observe time-dependent conformational change (27), but the method is a vibration intensity measurement. The method cannot provide information about the vibrational phase that could be obtained in the time-resolved absorbance change measurement. The vibrational phase enables us to distinguish between phenomena of the electronic ground state and those of the excited state.

As discussed in a recent study (14), time-resolved absorbance change measurements result from the contributions of wave packets on the potential surfaces of the electronic ground state and the excited state. There can be three ways to distinguish the ground state signal and the excited state signal. The first method is based on time-resolved spectroscopy and uses a chirped pump pulse as done by Kahan et al. (14). The second is to observe the vibrational phase of the molecular vibration. The ground state wave packet starts its motion from a stable local minimum point in the ground state potential energy surface, whereas the excited state wave packet starts its motion from Franck-Condon state toward a local minimum point in the excited state potential energy surface. Therefore, the vibrations of the wave packet along

the potential surfaces of the ground state and excited state are expected to be sine-like and cosine-like, respectively. The third method is to observe probe wavelength dependence and delay dependence of the signal. Because lifetimes of the intermediates are known from previous research, decay of the transient absorption signal clarifies which intermediate is dominant in each probe wavelength region. The sign of the signal also helps to assign the origin of the signal as follows: a negative absorbance change shows photobleaching caused by depletion of the electronic ground state or stimulated emission from the excited state; on the other hand, a positive absorbance change shows induced absorption from the first excited state to a higher excited state.

In this study, the experimental method of ultrafast spectroscopy performed in our previous work (26) was improved, including the second and third methods above, by using ultrashort laser pulses with the spectrum shown in Fig. 1 *a*. Experimental results include rich information on the sample dynamics, obtained from continuous spectra and time dependence (including vibrational phase) of transmittance changes at all wavelengths. Simultaneous measurement in all of the probe wavelengths can complete the measurement much faster than the previous time-consuming point-by-point (wavelength) measurements at five different wavelengths (26). Therefore, the simultaneous measurement suppressed systematic errors caused by long-term and short-term laser intensity fluctuation and also by sample degradation, which is inevitable in an experiment requiring a long time measurement.

The observed data revealed the photoexcited dynamics in the retinal chromophore of bR in full detail during the photoisomerization and could solve the above problems by the second and third methods above. Fig. 1 *b* shows the

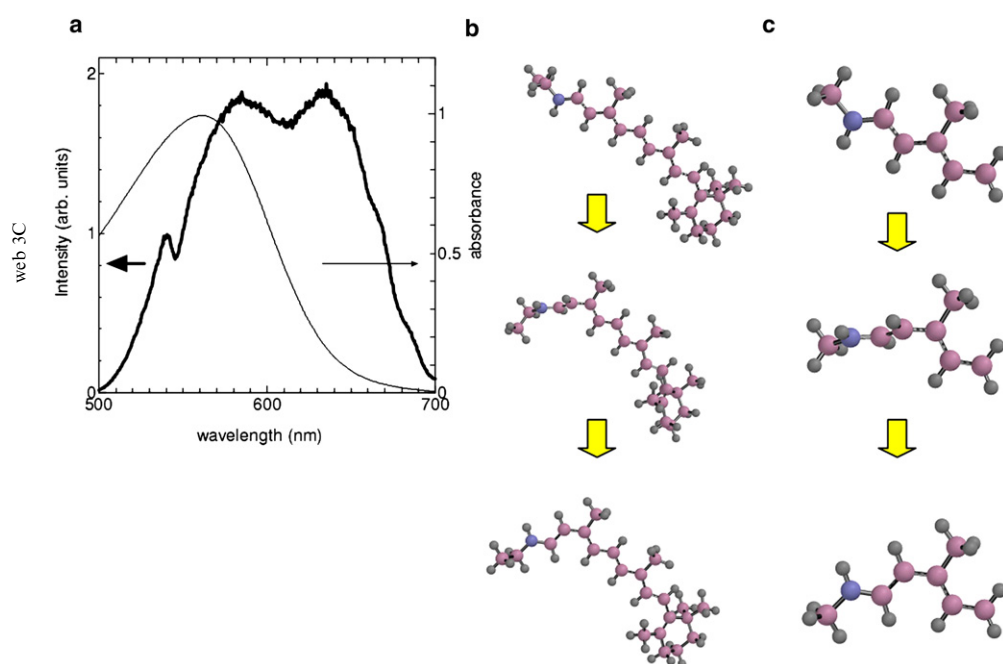


FIGURE 1 Laser spectrum, absorption spectrum of bR, and molecular structure of retinal in bR. (a) Laser spectrum (thick line) and absorption spectrum of bR (thin line). (b) Schematic conformational change in the *trans-cis* photoisomerization of the retinal chromophore in bR (CIS/6-31G\*/CIS/6-31G\*) (1). (c) Molecular structures around C<sub>13</sub>=C<sub>14</sub> and C<sub>15</sub>=N clipped out from *b*. In *b* and *c*, purple and blue spheres are carbon and nitrogen atoms, respectively. First, second, and third models in *c* are related to the structures of H, I, and J states, respectively.

structural change of retinal during the photoisomerization. Detail of the calculation method is shown in Material and Methods. The structural change in retinal was calculated to show a schematic image of structural change of retinyl chromophore in bR, and the calculated structure may have some differences in details when it is compared with the actual retinyl chromophore in bR, which is known to have largely twisted conformation even in K state (28,29). The time constants from the ground states to the intermediates I, J, and K were determined from the experimental results (see below) that are consistent with the results obtained in previous works by other groups (1,13,26,30). Then, probe wavelength dependence of the photoexcited dynamics was analyzed, and it was found that the probe wavelength spectrum can be classified into four spectral regions according to the dynamics. This is because the effects of the electronic states on each spectral region are different from each other. By the same reasoning, the dynamics of the molecular vibration modes was considered to be dependent on probe wavelength. Previously, Diller and colleagues (8) found that the C=N stretching mode appears earlier than 500 fs after the photoexcitation, and the present analysis of the molecular vibration modes shows the existence of a C=N stretching mode that decays within 30 fs after the photoexcitation, which means the primary event just after photoexcitation is neither the excitation of torsion around the C<sub>13</sub>=C<sub>14</sub> bond, as has long been believed (31), nor the C=C stretching mode, as was recently proposed (5). In the study presented here, it was finally concluded that the first process in the photophysical dynamics in bR is deformation of the retinal configuration, which decays within 30 fs near the C=N bond in the protonated Schiff base followed by the C=C stretching and then torsional motion of several periods around the C<sub>13</sub>=C<sub>14</sub> bond. The life of the mode is as short as 30 fs, corresponding to only 1.5 times of oscillation period (20 fs). This means that electronic redistribution just after excitation (<2 fs) triggers the fastest oscillation of C=N bond stretching, and the energy is then transferred to C=C stretching after a few oscillations of the former mode.

## MATERIALS AND METHODS

In this work, bR was suspended in water buffered at pH 7 without any detergent to use as a sample. The lifetime of the excited state is known to be different at pH >9, as reported by Logunov et al. (32). At pH 7, light-adapted bR mainly has an all-*trans* structure as reported in previous works (33,34). In Fig. 6 of Casadio et al. (33), absorption spectra of 13-*cis* and all-*trans* are peaked at 539 nm and 562 nm, respectively. The absorption spectrum of a bR sample (optical density per 1-cm OD<sub>1cm</sub> = 10.6 at the 560-nm peak in a 1-mm cell, and the laser spectra are shown in Fig. 1 *a*). The observed absorption spectrum with a peak at 562 nm confirms that the sample used in this work consists mainly of the all-*trans* structure. Fig. 1, *b* and *c*, shows the calculated structures of the retinal chromophore, which introduces the schematic mechanism of the *trans-cis* photoisomerization of the retinal chromophore. The geometry optimizations were performed with CIS/6-31\*\*/CIS/6-31\* (35) as shown in Appendix B. Models 1–3 in Fig. 1 *c* are related to the structures of the H, I, and J states, respectively. A noncollinear optical para-

metric amplifier (NOPA) was used to generate broadband visible pulses and compressed using a pulse compressor system, which can compress shorter than 4 fs (36). The details of NOPA and pulse compressor are given in Appendix A. Pump-probe signals were detected with a 128-channel lock-in amplifier. The energy and peak intensity of the pump pulses at the sample were ~10 nJ and 10 GW/cm<sup>2</sup>, respectively, which are ~10 times higher than the probe pulses. The laser spectrum is shown in Fig. 1 *a*.

## RESULTS AND DISCUSSION

As already mentioned, we present the ultrafast dynamics of the bR obtained from our experimental results in the following sections.

First, the ultrafast dynamics of “electronic states” was obtained from the measured transient absorption spectrum, and the time constants from the ground state to the intermediates H, I, and J were determined. The dynamics in each of four probe spectral regions was found to be different from each other, which means that they are caused by different mechanisms.

Further detailed analysis shows the ultrafast dynamics of “molecular vibration modes”. The dynamics was obtained by the calculation of instantaneous molecular vibration frequencies using the spectrogram analysis of the transient difference absorption spectrum. As is discussed in previous research (14), modes with frequencies close to each other interfere, resulting in artificial amplitude and/or frequency modulations in the spectrogram, the modulation frequency of which is equal to the difference between the interfering adjacent modes. However, all of the modulations discussed in this article are much lower than the frequency differences between the molecular vibration modes observed here. Therefore, those modulations in the spectrogram are concluded to be caused by real-mode coupling resulting in the periodic change in amplitude and/or frequency associated with conformational change in bR. The observed ultrashort lifetime of the C=N stretching mode leads to the conclusion that the primary event just after photoexcitation is the deformation of retinal configuration, which decays within 30 fs near the C=N bond in the protonated Schiff base followed by the C=C stretching and then torsional motion of several periods around the C<sub>13</sub>=C<sub>14</sub> bond. Below, we obtained vibrational phase spectra of C=C and C=N stretching modes, reflecting the contributing ratio between the phase of the wave packet motions in the electronic ground state with the phase of  $\pi/2$  or  $3\pi/2$ , and that in the electronic excited state with the phase of 0 or  $\pi$ .

### Ultrafast dynamics of electronic states

Fig. 2 *a* shows the two-dimensional (2D) trace of the time-resolved difference absorption spectra, obtained by averaging the spectra for 0.6 s (3000 laser shots). The 2D trace consists of 128 spectral data points over the 505–664 nm spectral region with a 1.25-nm step and 900 probe delay points between –100 and 800 fs with a 1-fs step.

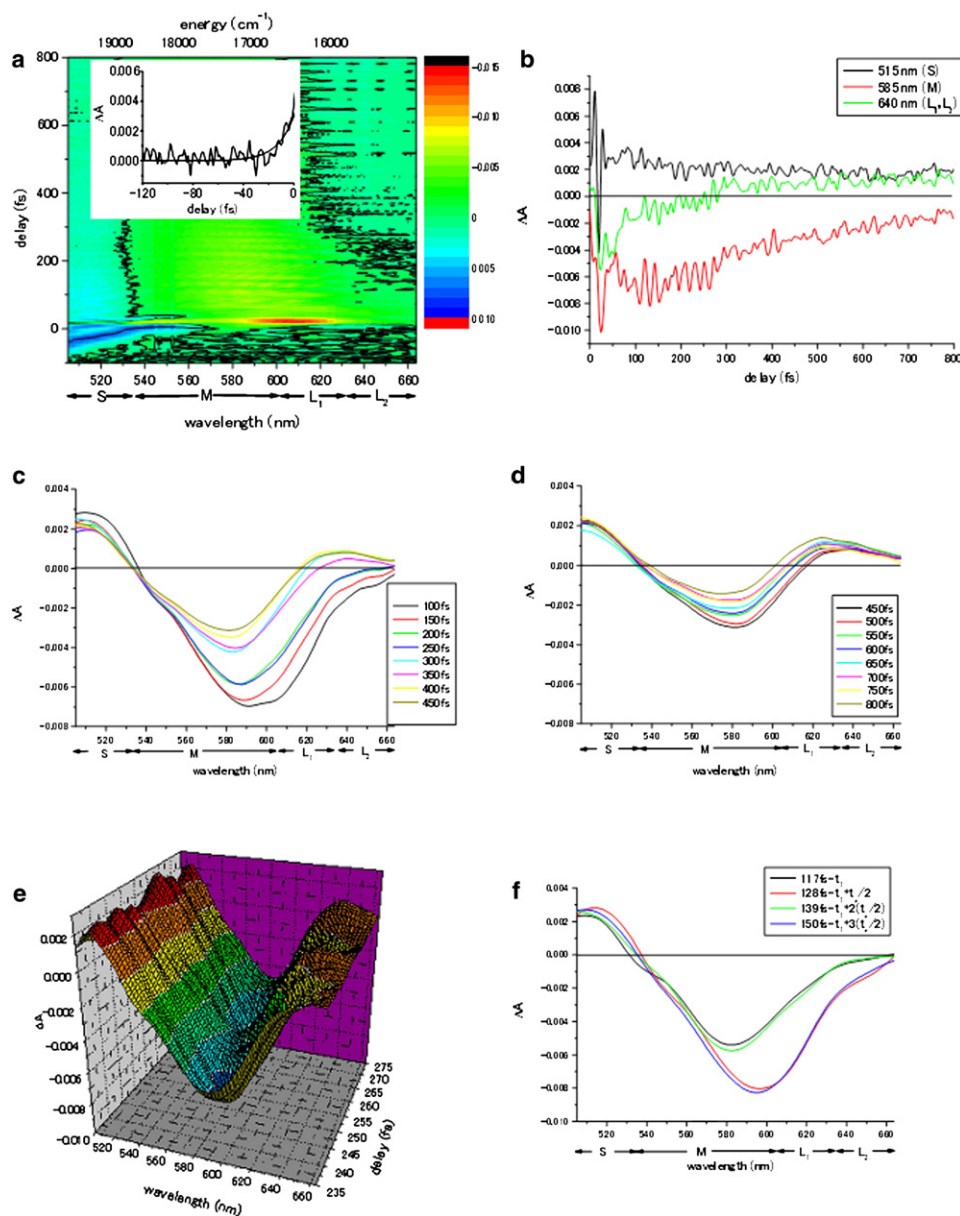


FIGURE 2 Time-resolved spectra of bR. (a) Measured 2D time-resolved spectra consisting of 128 data points in the 505–664 nm spectral region, and 900 data points with 1-fs steps between –100 and 800 fs delay time. Black lines correspond to  $\Delta A = 0$ . The peak of the signal in the negative delay time was shown as a thick black line as a hyperbolic function (37). Inset shows the  $\Delta A$  in the negative delay time region at 555 nm and a theoretical curve obtained for the perturbed free induction decay with the dephasing time of  $13 \pm 2$  fs. (b) Real-time traces of absorbance change at four probe wavelengths. Real-time difference absorption spectra at several delay times: (c) from 100 to 450 fs in 50-fs steps taken from the 1-fs step data, (d) from 450 to 800 fs in 50-fs step taken from the 1-fs step data. (e) The bird's-eye view of the 2D real-time difference absorption spectra from 235 to 275 fs with the 1-fs step. (f) Real-time difference absorption spectra at delay time between 117 and 150 fs with an interval of a half-period, 10.9 fs, of C=C stretching. S, M, L<sub>1</sub>, and L<sub>2</sub> show the labels of the four probe spectral ranges, labeled in ascending order of wavelength.

The transition time constants between the intermediates of the photoisomerization process were obtained by other groups (1,13,26,30) and explain the dynamics of the transient change of the difference absorption spectra observed in the 2D trace. From further analysis of the probe wavelength dependence of the signal, the ultrafast dynamics of the electronic states can be classified into four probe spectral ranges depending on their dynamics as follows.

The difference absorption spectra have different temporal and spectral behaviors in each of four probe wavelength regions, which consist of shorter (505–530 nm, S), middle (540–600 nm, M), and two longer (610–630 nm, L<sub>1</sub> and 635–664 nm, L<sub>2</sub>) wavelength ranges. The negative absorbance change ( $\Delta A < 0$ ) is caused by G-state depletion and partly by stimulated emission of HI state, which is the state

between H and I states (14). The positive absorbance changes ( $\Delta A > 0$ ) in S, L<sub>1</sub>, and L<sub>2</sub> ranges are well known to be caused by the induced absorption of the H, I, and J states (14,38). Signals observed in the negative time region show typical hyperbolic curves drawn in Fig. 2 a caused by the perturbed free induction decay (1,39), from which electronic dephasing time was estimated as  $13 \pm 2$  fs (see Fig. 2 a, inset), which is consistent with the width of the ground state absorption.

Fig. 2, b–d and f, show the real-time absorption changes as functions of delay time (b) and probe wavelengths (c, d, and f). Improved quality of the signal obtained by simultaneous measurement in the broad spectrum makes Fig. 2 b greatly superior to our previous results (26), which were affected by instability of laser spectrum and intensity in the long-time measurement. The increased number of spectral



measurement points from 5 to 128 makes the obtained data much more reliable and allows us to repeat experiments to check the reproducibility in a very short measurement time.

Fig. 2, *c* and *d*, shows that the photoexcited dynamics of bR in S, M, L<sub>1</sub>, and L<sub>2</sub> spectral ranges can be explained as follows. In the S spectral range, the signal decays partially in ~200 fs, and residual intensity remains to have longer life than 1 ps (data not shown). The decay process corresponds to the induced absorbance changes from the transformation from the H state into the I state. The long-life component can be assigned to the induced absorption spectra caused by the I and J states in the S spectral range. In Fig. 2 *c*, the absorbance change in the S spectral range decays over 100–400 fs. This can be assigned to the signal of the I state, which is known to decay in 0.7 ps after photoexcitation (41). The absorbance change in Fig. 2 *d* keeping almost the same intensity during 400–800 fs shows the existence of a long-lifetime component. It was attributed to the J state, whose lifetime is known to be 3 ps (41). In the M spectral ranges, the negative  $\Delta A$  signal results from ground (G)-state depletion and partly from the stimulated emission of the HI state. The G-state depletion also partly affects the signal in L<sub>1</sub> range because the ground state absorption is nonnegligible ( $0.2 < \text{O.D.} < 0.5$ ). In the L<sub>1</sub> and L<sub>2</sub> ranges, the  $\Delta A$  monotonically increases until 200 fs because of the disappearance of stimulated emission of the HI state and the appearance of the induced absorption of the I state. The time constant of 200 fs is consistent with the reference value(s) of the H state lifetime (42). The induced absorption of the I state with a peak at 460 nm contributes more effectively in the L<sub>1</sub> range than in the L<sub>2</sub> range. Then around 200 fs after excitation, the  $\Delta A$  spectrum still grows with its peak close to the absorption peak wavelength of the J intermediate (625 nm) in the L<sub>1</sub> and L<sub>2</sub> ranges, which has a longer life than signals related to other (G, H, and I) states. The  $\Delta A$  spectrum (Fig. 2, *c* and *d*) shows the real-time dynamics of bR that is converted into J intermediate in ~700 fs.

The 2D display of difference absorption spectra between 235 and 275 fs shown in Fig. 2 *e* exhibits the periodic changes in both peak intensities and the steepness of the difference absorption spectra. The period of the changes mainly reflects the molecular vibration period of the C=C stretching mode. As a clear indication of the periodicity of the spectral change, the snapshots of difference absorption spectra are displayed in Fig. 2 *f* with an interval of half of the C=C stretch period,  $t_p/2 = 11$  fs. The spectral changes shown in the figure correspond to the spectral changes observed between two turning points on the potential surface of the C=C stretching mode.

### Ultrafast dynamics of vibrational modes

The Fourier power spectra of real-time traces of absorbance changes reveal that photoexcitation of the sample causes vibronic coupling and several molecular vibration modes

are excited in the sample. Referring to the reported Raman shifts (4,42–45), the signals around 1520 and 1640  $\text{cm}^{-1}$  were attributed to the C=C and C=N stretching modes reported as 1527 and 1640  $\text{cm}^{-1}$ , respectively. The Fourier amplitude of the “C<sub>13</sub>=C<sub>14</sub> stretching mode” is considered to be the linear combination of the amplitude of C<sub>13</sub>=C<sub>14</sub> stretching and of other C<sub>*i*</sub>=C<sub>*i*+1</sub> (*i* = 7, 9, 11) stretching. The subscript *i* refers to the position of the carbon atom in the molecule. Whether these modes result from the wave packets in the ground state, the excited state, or the intermediate state is addressed later by analyzing in detail the frequency of each mode as functions of delay time and probe wavelength. As we observed in our previous work (26), the signals around 1000 and 1250  $\text{cm}^{-1}$  were also observed and attributed to “the hydrogen out-of-plane (HOOP) mode” (18,46–48) and “the in-plane C=C-H bending mode coupled with C-C stretching mode”, respectively.

To study the dynamics of the molecular vibration modes, the delay time dependences of frequency and amplitude of the above vibration modes were analyzed throughout the probe wavelength range using a spectrogram technique (14,49). The spectrogram traces were obtained by a gated Fourier transform (FT) with a Blackman window of 120 fs half-width at half-maximum, shown in Fig. 3. The sliding-window FT with a short width causes the broad frequency width of the peaks in the spectrograms (14). In the following analysis, the effect of the finite width was deconvoluted to determine time constants.

#### *Dynamics of the HOOP mode and the in-plane C=C-H bending mode coupled with C-C stretching mode*

Periodic intermixing between the HOOP and in-plane C=C-H bending modes suggests that they are modulated by the structural change of the molecule in the photoisomerization during and after passing through the conical intersection and/or transition state. The I state is considered to have a twisted structure around C<sub>13</sub>=C<sub>14</sub>. The twist around the bond lowers the symmetry of the molecule and mixes the out-of-plane (HOOP) mode and in-plane (C=C-H bending) mode and causes the intermixing of these modes. Therefore, the first intermixing observed at ~200 fs in Fig. 3, *d–f*, reflects the appearance of the I state. The growth time of the I state is consistent with the results shown by other groups (1,6,13). Recovery of the C-C stretching mode signal at ~700 fs was clearly observed in the spectral ranges of L<sub>1</sub> and L<sub>2</sub> (Fig. 3, *e* and *f*) because of the narrowing of the torsion angle distribution in the quasi-thermal state (J intermediate) after relaxing to the bottom (or the point close to the conical intersection) of the potential curve along the C<sub>13</sub>=C<sub>14</sub> torsion angle coordinate (26). The reason the signal is detectable only in the spectral ranges of L<sub>1</sub> and L<sub>2</sub> is that the absorption peak wavelength of the stable J intermediate, 625 nm, is close to the L<sub>1</sub> and L<sub>2</sub> ranges. The observed J intermediate growth time (~700 fs) is also consistent with previous results (1,6,13,41).

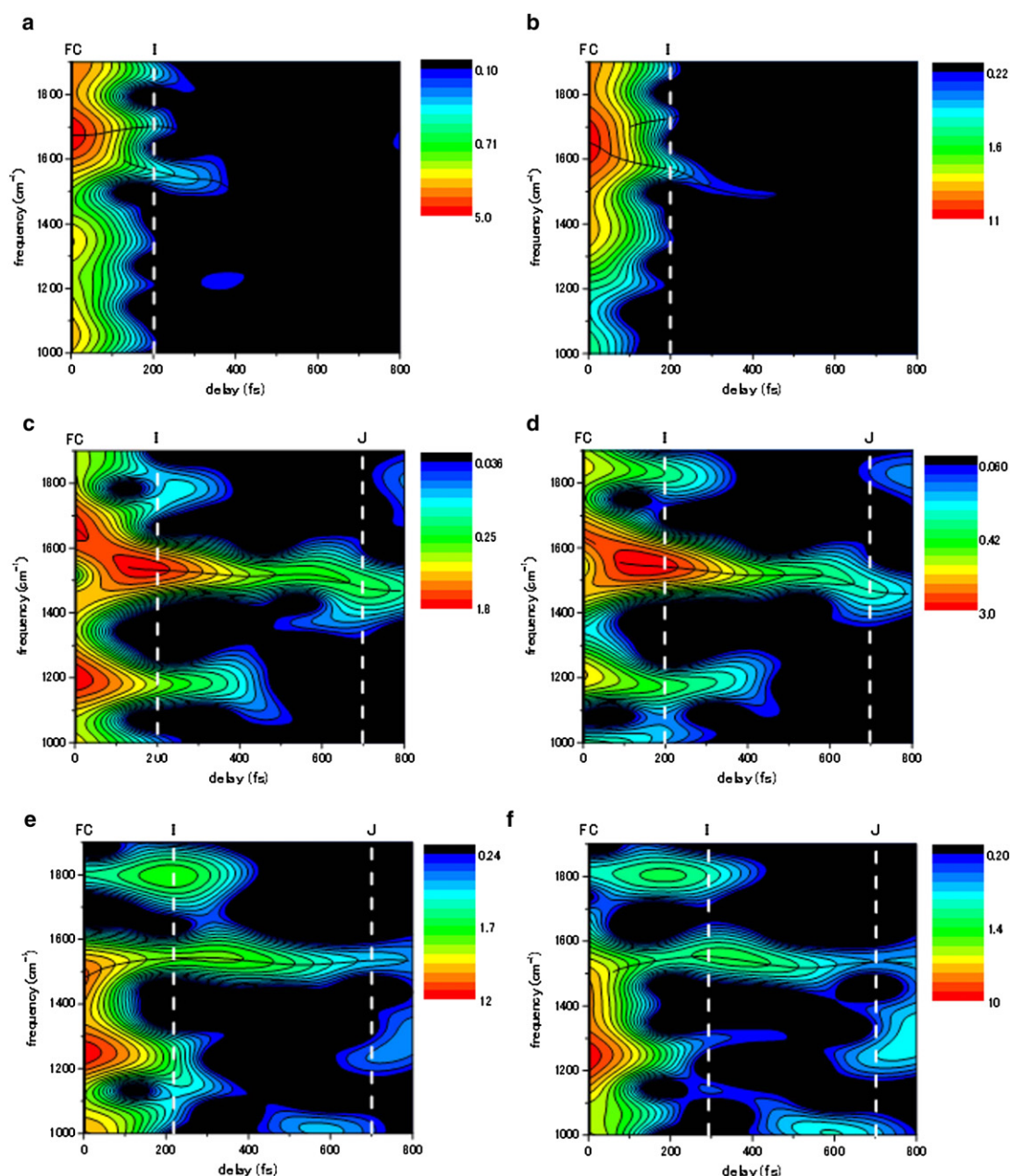


FIGURE 3 Spectrograms calculated from the real-time traces measured at (a) 512 nm, (b) 517 nm, (c) 572 nm, (d) 577 nm, (e) 617 nm, and (f) 622 nm. White broken lines in the figures show the approximate appearance time of the H, I, and J states.

The C=C stretching modes observed in Fig. 3, c and d, change their frequencies lower at  $\sim 700$  fs, which implies that the C=C stretching mode frequency of the J intermediate (13-*cis* structure) is lower than those of the other (G, H, and I) states, which have all-*trans* or twisted structure.

*Real-time modulation of the C=C stretching mode reflecting the change of C=C bond length*

The spectrogram traces show the instantaneous vibration frequency and amplitude of the C=C stretching mode. The modulation of the instantaneous frequency of the C=C stretching

mode reflects the molecular (bond length) deformation during the photoisomerization process as discussed in this section.

Fig. 4 a is the spectrogram that is clipped from Fig. 3 around the frequency of the C=C stretching mode, from 1450 to 1750  $\text{cm}^{-1}$ , showing that the instantaneous frequency of the C=C stretching mode,  $\nu_{\text{C}=\text{C}}$ , is periodically modulated. The modulation,  $\Delta\nu_{\text{C}=\text{C}}$ , of stretching mode frequency implies that the bond order and bond length of  $\text{C}_{13}=\text{C}_{14}$  are periodically changing during the torsion around the  $\text{C}_{13}=\text{C}_{14}$  during and after passing through the conical intersection and/or transition state (26). The periodic change was also observed in a recent model study of the population

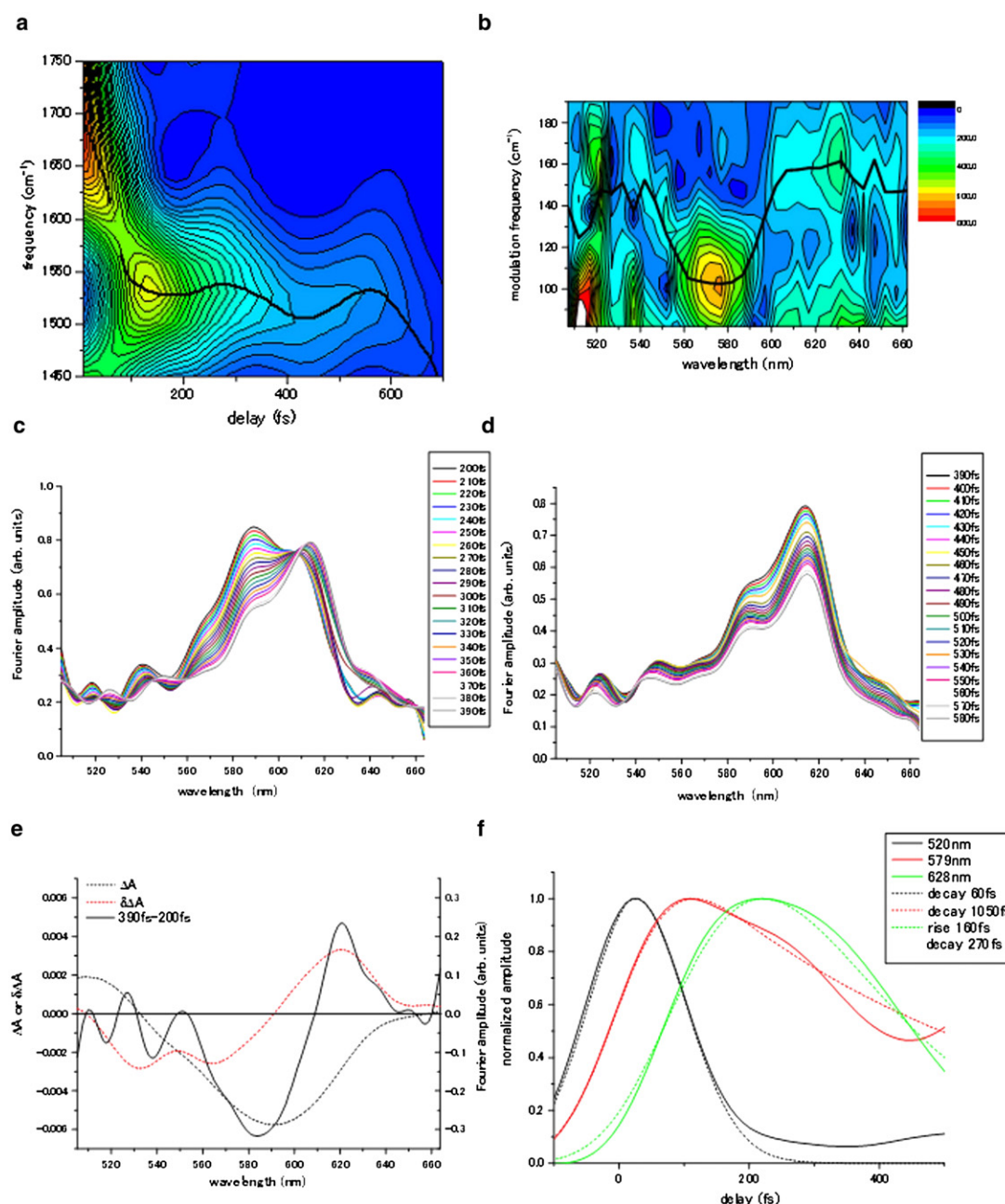


FIGURE 4 Ultrafast dynamics of the probe wavelength dependence of the Fourier amplitude (Fourier amplitude spectrum) of the C=N and C=C stretching modes during the photoisomerization process of bR. (a) 2D (the frequency and gate delay) display of the frequency and amplitude modulations of the C=C stretching mode frequency in the spectrogram measured at 572 nm. (b) 2D Fourier amplitude spectra of the instantaneous frequency of C=C stretching mode, which show the modulation frequency of C=C stretching frequency at each probe photon energy. This clearly shows that the modulation frequency is different among four probe wavelength ranges (S, M, L<sub>1</sub> and L<sub>2</sub>). (c) Fourier amplitude spectra of the C=C stretching mode in the time range between 200 and 390 fs. (d) Fourier amplitude spectra of the C=C stretching mode in the time region from 390 to 580 fs. (e) Difference absorption spectrum at the delay of 200 fs (black dotted curves) and its first derivative (red dotted curves). Black solid curve shows the difference Fourier amplitude spectrum between 200 fs delay and 390 fs delay. (f) Fourier amplitude traces of the C=C stretching mode at three probe wavelengths (solid curves) and the numerical fit (dotted curves).

of the photoisomerized retinyl chromophore (19). In the same manner as the electronic state dynamics, the modulation amplitude of stretching frequency showing the dynamics of the C=C stretching mode can also be classified in the same way as HOOP mode dynamics into the four probe wavelength ranges of S, M, L<sub>1</sub>, and L<sub>2</sub> as follows.

The modulation period,  $\tau(\Delta\nu_{C=C})$ , and modulation amplitude,  $|\Delta\nu_{C=C}|$ , of the C=C stretching frequency in each probe wavelength was studied by calculating the Fourier amplitude spectra of the time-dependent instantaneous frequency of the C=C stretching mode (see Fig. 4 b) from the spectrograms. The frequency in which the C=C



stretching frequency is modulated,  $\tau(\Delta\nu_{C=C})$ , was estimated to be  $142 \pm 35$ ,  $105 \pm 3$ ,  $158 \pm 3$ , and  $150 \pm 18$   $\text{cm}^{-1}$  in S, M,  $L_1$ , and  $L_2$  ranges, respectively. The modulation amplitude of the C=C stretching frequency reflects the size of the  $C_{13}=C_{14}$  bond length change. Applying the observed modulation amplitude to an empirical equation of Baughman et al. (50), which represents the relation between the bond length and frequency, enables us to estimate the change in the bond length of  $C_{13}=C_{14}$  to be  $27 \pm 7$ ,  $18 \pm 2$ ,  $20 \pm 3$ , and  $27 \pm 5$  mÅ in S, M,  $L_1$  and  $L_2$  ranges, respectively, correcting the reduction of modulation amplitude by the finite gate width used in the spectrogram. In this analysis, we have used the data between the delay time of 100 fs and 700 fs; therefore, the result is contributed by the G, I, and J states. The dominantly contributing states in each spectral range in this time regime can be summarized as follows. In the S, M, and  $L_{1,2}$  spectral ranges, I state, G state, and I and J states are dominant, respectively.

In regard to the above classification of the dominant states in each spectral range, we come to the conclusion that the changes in bond length of  $C_{13}=C_{14}$  in the G state, J state, and I state are  $18 \pm 2$ ,  $20 \pm 3$ , and  $27 \pm 7$  mÅ, respectively.

#### *Wavepacket motion observed by transient change of the C=C stretching mode spectrum*

A cross section along the gate-delay time axis of the spectrogram shows a time-resolved Fourier amplitude spectrum that is changing during the photoisomerization. In this section, the observed time-dependent amplitude of C=C stretching mode was used for the determination of the transition time constants between the intermediates, and the deformation of the Fourier power spectrum showed the wave packet motion in the photoisomerization.

Fig. 4, c and d, shows the delay time dependence of the amplitude spectra of C=C stretching mode calculated from the spectrograms. It is known that the H state is already transformed into the I state 200 fs after excitation, and the decay time of the G state wave packet is as long as ~1 ps or longer. Therefore, the fast spectral change in Fig. 4 c indicates the decay and growth of a wave packet on the potential surfaces of the I state (contributing to S and M spectral ranges) and that of the J intermediate ( $L_{1,2}$  spectral ranges), respectively, with ~200 fs time constant. This growth of vibrational coherence is another example of reaction-driven coherence previously observed in MbNO (51). The continuous change of the Fourier amplitude spectrum represents the change in the vibronic-coupling strength spectrum during the transformation from the I state to the J intermediate without any other state between them.

The difference between the Fourier amplitude spectrum at 200 fs and that at 390 fs is depicted with a solid black line in Fig. 4 e. This shows that the signal intensities of the C=C stretching mode in the spectrograms at the wavelengths of 590 and 620 nm are changing in an anticorrelated way with the existence of an isosbestic point at 605 nm in the

time range of 200–390 fs. These two wavelengths (590 and 620 nm) are very close to the corresponding peak of the difference absorption spectrum (584 nm) and that of its derivative (620 nm), as shown in Fig. 4 e. This is because the vibration modes are most sensitive at the peak of the difference absorption spectrum, and spectral change from a time-dependent Franck-Condon factor induced by the wave packet motion is most intense at the peak of the first derivative of the difference absorption spectrum (51). This is well explained in terms of the transient spectral shift associated with the wave packet motion in general in the molecular systems as discussed in a previous study (52).

#### *Dynamics of the C=C stretching mode*

The behavior of the delay time dependence of the Fourier amplitude (FT amplitude trace) of the C=C stretching mode, obtained from the spectrograms, was used for the analysis of the dynamics of the C=C stretching mode, which is studied in this section.

Similarly to the case of electronic-state dynamics, the dynamics of the C=C stretching mode can also be classified into the probe wavelength ranges (Fig. 4 f). As mentioned previously in this article, the G, H, and I states can be observed in the time range up to 500 fs shown in Fig. 4 f. Dominantly contributing states in each spectral region in this time range can be summarized in the next sentence. In the S, M, and  $L_{1,2}$  spectral ranges, “the H and I states”, “the G state”, “the H and I states” are dominant, respectively.

The Fourier amplitude trace in the S range has only a small contribution of long-life component from the I state. Therefore, the signal is considered to be mainly from the induced absorption of the H state. From further analysis including a rise time as another fitting parameter (not shown here), we found that the signal appears with a delay of ~14 fs after photoexcitation. The Fourier amplitude in the M range indicates that the signal comes from the depletion of the G state. On the other hand, the Fourier amplitude traces in the  $L_1$  spectral range mainly include both the signals from the induced emission of the HI state and the one from the induced absorption of the I state, as is also expected from the 2D time-resolved spectrum shown in Fig. 2 a. The latter signal can then be obtained by decomposing the Fourier amplitude trace. After subtracting the contribution of depletion in  $L_{1,2}$  spectral ranges, we obtained FT traces in the S, M, and  $L_1$  ranges (see Fig. 4 f), of which signals are mostly from the induced H-state absorption (S), the G-state depletion (M), and the induced I-state absorption ( $L_1$ ), respectively. The FT trace of  $L_2$  is similar to that of  $L_1$  in the time region of Fig. 4 f; therefore, it was omitted from the figure.

To determine the time constants of the dynamics, we fitted the traces in Fig. 4 f with curves numerically calculated, assuming that the vibration amplitude has exponential growth and decay dynamics. The decay constants of the vibration amplitudes of C=C stretching in the H and G states were estimated to be  $< \sim 100$  fs and  $1050 \pm 180$  fs,

respectively, by simulation in the S and M ranges. The simulated curve for  $L_1$  spectral range shows that the rise time constant caused by the I state population and the decay time constant of C=C stretching amplitude of the I state are  $160 \pm 20$  and  $270 \pm 30$  fs, respectively. The latter decay is much shorter than the 500-fs decay of the I state (1,6,13). This fast decay is attributed to the modulation of C=C bond length by torsion (26), which enhances the mode mixing with other modes and results in the dissipation of the vibration energy of the mode. The long decay time of  $\sim 1$  ps in M spectral range indicates that the ground state contribution to the transition modulation is more effective than the other (H and I) states in M spectral range, as expected from the strong absorption of the ground state in comparison with the absorption of the transient (H and I) states. There is some deviation of the experimental results from the fitting curves in Fig. 4 *f*. This is probably a result of probe-wavelength-dependent decay time because of a possible small but wavelength-dependent mixed contribution(s) of wave packets in the G, H, and I states.

*Ultrafast (<30 fs) dynamics of the C=N stretching mode just after photoexcitation*

The earlier delay time range of the spectrogram was studied to observe the initial dynamics just after the photoexcitation.

The spectrograms in the S and M spectral ranges (Fig. 3, *a–d*) show the existence of the C=N stretching mode with frequency of  $\sim 1640$   $\text{cm}^{-1}$  corresponding to 20 fs. The C=N signal in the spectrogram quickly disappears in 30 fs. Because of the short lifetime of the mode corresponding to the 1.5 oscillation periods, the Raman spectrum is expected to have a broad bandwidth, as broad as  $1100$   $\text{cm}^{-1}$ , resulting in the reduction of peak intensity by the factor of  $\sim 100$  estimated from the width of Raman spectrum of C=N mode in the ground state (38). This makes it practically impossible to be observed in the Raman spectrum. From the line width of the ground state Raman signal of bR (38), the decay time of the C=N stretching mode in the ground state was known to be a little longer than 3 ps, whereas the observed C=N signal decays much faster (<30 fs) than the appearance time (>200 fs) of the I state. Therefore, the observed Fourier signal of the C=N stretching frequency is thought to be caused neither by the G state nor by the I state but by the H state, which is excited in the very first process of photoisomerization. The excited molecular vibration of the C=N stretching mode decays rapidly (<30 fs) in the H state, indicating that the oscillation of C=N vibration bond length takes place less than twice. The H state then decays with the time constant of  $235 \pm 22$  fs. This finding can explain the very interesting but controversial observation by Ruhman's group (15) in the following way. Even the locked retinal analog can undergo the deformation near the protonated C=N bond, leading to a spectral change close to that induced by the isomerization. Therefore, the spectral changes commonly observed both in native retinal and in the artificial locked analog is introduced

by the electronic changes not near the  $C_{13}=C_{14}$  bond but near the protonated C=N bond. After this conformation change near the C=N bond, the vibration of which is heavily damped, C=C stretching and then torsion around  $C_{13}=C_{14}$  bond starts.

As was studied by Mathies and co-workers (1), the I state appears within  $\sim 200$  fs. The positive  $\Delta A \sim 200$  fs after excitation in  $L_1$  and  $L_2$  spectral ranges shows the contribution of the induced absorption by the I state. In the probe spectral ranges, a new signal around  $1800$   $\text{cm}^{-1}$  is found to appear around 200 fs after excitation (Fig. 3, *e* and *f*), indicating that the signal is mainly from the I state. This new mode is possibly related to highly distorted C=N stretching. The increase in the frequency of C=N to  $\sim 1800$   $\text{cm}^{-1}$  indicates that the  $\pi$ -electron flow to the protonated Schiff base after the very rapid distortion partly neutralizes the positive charge of N (nitrogen atom), resulting in the increase of bond order. It implies that the charge redistribution arises from interaction with binding pocket residues, and the distortion relaxes on formation of the J intermediate.

**Vibrational phase spectra of the C=C and C=N stretching modes**

In this work, we obtained an ultrafast time-resolved pump-probe signal that can resolve real-time molecular vibration to reveal the phase spectra of molecular vibration modes. The phase spectra, which cannot be obtained by common time-resolved Raman spectroscopy, provide valuable clues to determine whether the electronic ground state or excited state is contributing to the dynamics of the molecular vibration modes.

Fig. 5 shows the phase spectra of the C=C and C=N stretching modes obtained by the Fourier transform of the measured 2D trace between the delay time of 100 fs and

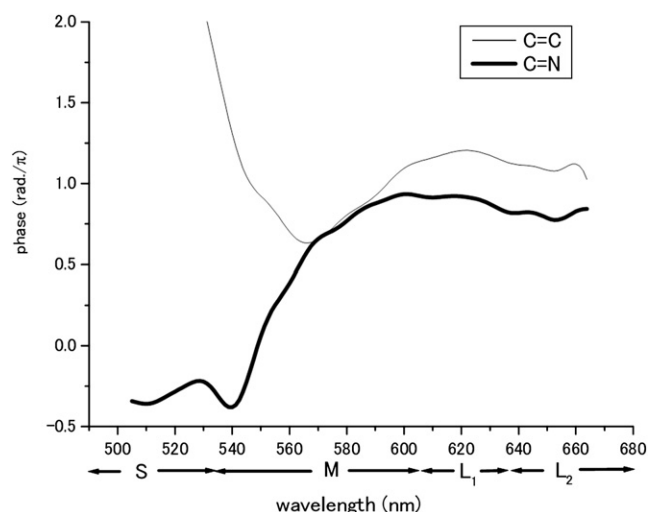


FIGURE 5 Probe wavelength dependence of vibrational phase (phase spectra) of the C=C stretching mode (*thin lines*) and C=N stretching mode (*thick lines*) obtained from the Fourier transform of the data between the delay time of 100 fs and 800 fs.

800 fs. The features of the phase spectra can also be classified into the wavelength ranges. The phase of the C=C stretching mode is within  $\pi/8$  of  $\pi/2$  in the M spectral range, whereas it is within  $\pi/10$  of  $\pi$  in the  $L_1$  and  $L_2$  ranges. These indicate that the contribution of the wave packet motion along the ground-state potential is more effective (74%) than that of the excited state (26%) in the M spectral range, and it penetrates into the L spectral range. The phase in the S range dramatically changes from  $\sim 2\pi$  to  $0.5\pi$  with a kink at  $1.0\pi$  around 540 nm, which is close to the  $\Delta A$  zero-crossing point (Fig. 2 c). In the zero-crossing range the phase jump of  $\pi$  indicates in-phase instead of out-of-phase modulation of induced absorption and bleaching, with opposite signs (52) found in the J aggregates in which dynamic intensity borrowing is taking place. The closest value of the phase to  $\pi/2$  is located at 560 nm, corresponding to the peak of the ground-state absorption, where the highest contribution of the ground-state wave packet is expected. Therefore, it can be concluded that a wave packet on the excited-state potential is most effectively contributing to the S spectral range and also penetrates into the M range.

In Fig. 5, the phase of the C=N stretching mode is within almost  $\pi/4$  of  $0\pi$  in S spectral range and is within almost  $\pi/10$  of  $\pi$  in M and L ranges. Therefore, the phase spectrum supports the assignment of the signals of the C=N stretching mode to the excited-state wave packet together with the decay time of the vibration amplitude, as discussed before.

## CONCLUSION

We have observed the real-time molecular vibrations with a few optical cycle laser pulses and a 128-channel simultaneous detection system over the spectral range of 505–664 nm to get quasicontinuous spectra of transient signals with ultrahigh time-resolution, which can real-time resolve molecular vibration. Our experimental results revealed that the first configuration change takes place in a C=N bond and then the modulation of stretching frequency of C=C, followed by the distortion around the C=C bond resulting in the isomerization.

Probe wavelength dependence of the time-resolved difference absorption spectrum shows that each of four probe spectral ranges has four different dominant electronic state dynamics. The spectrograms calculated in every probe wavelength clearly visualized the dynamics of vibration modes of the photoexcited bR, which transforms into the H, I, and J states. Change of molecular structure during the photoisomerization causes the intermixing between the HOOP mode and the in-plane C=C-H bending mode. The real-time modulation of C=C mode frequency (Fig. 4 a) indicates that the C=C bond length is modulated by  $\sim 20$  mÅ during the photoisomerization around  $C_{13}=C_{14}$  bond. The rapid spectral change in Fourier amplitude spectra of the C=C stretching mode (Fig. 4 a) reflects the real-time wave packet motion during the transformation process from the I state to the J intermediate. FT traces were analyzed to determine the

timescale of the dynamics of the induced H-state absorption, the G-state depletion, and the induced absorption of the I state. The earlier delay range of the spectrogram was studied to observe the initial dynamics just after the photoexcitation and found the C=N stretching mode, which quickly disappears with a decay time constant of  $<30$  fs. The Fourier phase spectra of C=C and C=N modes have clarified that each of the C=C and C=N modes in each spectral range is related to the wave packet of either the ground state, the excited state, or intermediates (Fig. 5).

Analyzing the modulation of vibration modes, we found that ultrafast dynamics during photoisomerization of bR can be summarized as follows. Just after the photoexcitation, the C=N stretching mode was found to be excited, showing that the primary event just after photoexcitation is a deformation of retinal configuration, which decays within 30 fs near the C=N bond in the protonated Schiff base. Observed dynamics of the molecular vibration modes in four spectral regions showed that signals in these spectral regions are dominated by different intermediates during the photoisomerization. The result elucidated dynamics of the intermediates, whose lifetimes are consistent with previous reports.

The work presented here can easily be applied to observe the ultrafast structural changes during and after passage through the conical intersection and/or transition state even in the ground state. This can be realized by utilizing a chirp-controlled excitation pulse to generate a wave packet in the ground state. It can also be applied to a complex system, such as femtosecond configuration dynamics of proteins, which is useful in the field of medical and biological sciences where optical probing is increasingly important.

## APPENDIX A: NONCOLLINEAR OPTICAL PARAMETRIC AMPLIFIER

The source laser of the pump-probe spectroscopy system is a regenerative chirped pulse amplifier (CPA1000; Clark-MXR, Dexter, MI) seeded with a fiber laser oscillator. The amplifier generates femtosecond pulses whose duration, central wavelength, repetition rate, and average power are 120 fs, 790 nm, 1 kHz, and 400 mW, respectively. The ultrashort 1-kHz pulse train used for the ultrafast time-resolved pump-probe spectroscopy of bR was generated by a NOPA. The NOPA generates amplified pulses with a broad bandwidth of  $6000\text{ cm}^{-1}$  in the visible spectral range, which is enough to support sub-4-fs operation. A special phase-matching condition, which is called the “magic” phase-matching condition, enabled us to generate amplified visible pulses whose bandwidth was extremely broad, 200 THz, using a Type-I BBO ( $\beta\text{-BaB}_2\text{O}_4$ ) crystal pumped by 400-nm laser pulse. To satisfy the phase-matching condition, the direction of a pump beam should be inclined  $\sim 3.7^\circ$  to that of a seed beam, and the inclination angle coincidentally matches the walk-off angle between the ordinary and extraordinary waves inside the crystal. Therefore, we could use a 1-mm-thick BBO crystal for the NOPA process in our experimental setup. The thickness and cutting angle of the BBO crystal for NOPA were 1 mm and  $31.5^\circ$ , respectively. The optimum inclination angle between the pump and seed beams is dependent on the pump wavelength. Therefore, we put a Brewster-angled prism in the light path of the pump beam to cause angular dispersion in the pump beam and enhance the phase-matching bandwidth of NOPA. The prism was placed 800 mm in front of the  $R = -200$  mm mirror,

TABLE 1 Reactant

Center number	Atomic number	Atomic type	Coordinates (Å)		
			X	Y	Z
1	1	0	-0.451168	0.121416	-0.189496
2	6	0	-0.256594	0.032229	0.877981
3	1	0	0.813865	-0.160711	0.960431
4	6	0	-0.985927	-1.186753	1.381355
5	6	0	-1.676050	-1.190125	2.561064
6	6	0	-1.611358	-0.001704	3.555756
7	6	0	-0.574408	1.046183	3.107079
8	1	0	0.422495	0.697470	3.368047
9	1	0	-0.738462	1.959393	3.669839
10	6	0	-0.612501	1.315292	1.611128
11	1	0	-1.594868	1.660802	1.304741
12	1	0	0.090894	2.097481	1.346371
13	6	0	-3.003725	0.653149	3.659642
14	1	0	-2.984234	1.468452	4.375943
15	1	0	-3.752362	-0.058717	3.992948
16	1	0	-3.335087	1.051050	2.707025
17	6	0	-1.183629	-0.482006	4.958391
18	1	0	-0.274342	-1.072766	4.913716
19	1	0	-1.946189	-1.066448	5.460791
20	1	0	-0.988610	0.379850	5.588018
21	6	0	-2.508188	-2.286428	2.977777
22	6	0	-3.212704	-3.165370	2.179528
23	1	0	-3.195673	-3.009178	1.118778
24	6	0	-4.028342	-4.224450	2.627321
25	6	0	-4.771588	-4.914508	1.654038
26	1	0	-4.645280	-4.599517	0.632606
27	6	0	-5.667411	-5.955501	1.886141
28	6	0	-6.362074	-6.585317	0.849644
29	1	0	-6.171931	-6.233473	-0.149677
30	6	0	-7.280411	-7.632437	0.992710
31	6	0	-7.882123	-8.141364	-0.174254
32	1	0	-7.594158	-7.688566	-1.108086
33	6	0	-8.804758	-9.166356	-0.237651
34	7	0	-9.345299	-9.621569	-1.356749
35	1	0	-9.074640	-9.188089	-2.214881
36	6	0	-10.338536	-10.684920	-1.445015
37	1	0	-10.421503	-11.137130	-0.465343
38	1	0	-9.964597	-11.446703	-2.119724
39	6	0	-11.694595	-10.172221	-1.918274
40	1	0	-12.093969	-9.436609	-1.229377
41	1	0	-12.396668	-10.995815	-1.988515
42	1	0	-11.618887	-9.715619	-2.899725
43	1	0	-9.138731	-9.665566	0.651394
44	6	0	-7.585440	-8.168316	2.370751
45	1	0	-7.973444	-7.379163	3.006972
46	1	0	-6.683337	-8.553053	2.836130
47	1	0	-8.312184	-8.965988	2.367181
48	1	0	-5.832522	-6.281482	2.894797
49	6	0	-4.135309	-4.620701	4.077441
50	1	0	-5.095431	-4.320137	4.489296
51	1	0	-3.357258	-4.184051	4.684700
52	1	0	-4.055809	-5.697178	4.183659
53	1	0	-2.676466	-2.360321	4.033470
54	6	0	-0.796015	-2.378839	0.478812
55	1	0	0.210064	-2.356003	0.071399
56	1	0	-1.471341	-2.330993	-0.374214
57	1	0	-0.935345	-3.325712	0.977984

Hartree-Fock = -97.0878889 Hartree; Möller-Plesset second-order perturbation = -910.0616618 Hartree. Excited state, 1: 2.8572 eV; 433.93 nm;  $f = 2.4328$ . Zero-point correction = 0.547638 (Hartree/particle). Thermal correction to Gibbs free energy = 0.487555.



TABLE 2 Transition state

Center number	Atomic number	Atomic type	Coordinates (Å)		
			X	Y	Z
1	1	0	0.253860	−0.206052	0.069459
2	6	0	0.172673	−0.141759	1.152367
3	1	0	1.189328	−0.250964	1.529107
4	6	0	−0.641899	−1.320210	1.641099
5	6	0	−1.569515	−1.206975	2.600746
6	6	0	−1.856079	0.113836	3.348952
7	6	0	−0.771519	1.162557	3.039457
8	1	0	0.120724	0.929401	3.616770
9	1	0	−1.115835	2.134444	3.380568
10	6	0	−0.393538	1.208450	1.566423
11	1	0	−1.259590	1.449522	0.957465
12	1	0	0.339161	1.989108	1.388094
13	6	0	−3.242356	0.645619	2.933746
14	1	0	−3.478059	1.555598	3.477637
15	1	0	−4.021560	−0.078547	3.149611
16	1	0	−3.287525	0.866611	1.873254
17	6	0	−1.857644	−0.101627	4.876091
18	1	0	−0.956056	−0.609004	5.206063
19		0	−2.715521	−0.670414	5.218475
20		0	−1.897849	0.859906	5.377634
21		0	−2.400469	−2.353430	3.027362
22	1	0	−3.109103	−3.147458	2.212224
23	1	0	−3.082672	−2.955192	1.154488
24	6	0	−3.942317	−4.259632	2.634735
25	6	0	−4.598561	−4.960907	1.663458
26	1	0	−4.465834	−4.629273	0.647785
27	6	0	−5.437572	−6.089984	1.840128
28	6	0	−6.102918	−6.687998	0.788668
29	1	0	−5.918108	−6.296416	−0.196500
30	6	0	−6.982335	−7.774828	0.895279
31	6	0	−7.452241	−8.412795	−0.301828
32	1	0	−7.042207	−9.367724	−0.608625
33	6	0	−8.431876	−7.850900	−1.136424
34	7	0	−8.802360	−8.353665	−2.284250
35	1	0	−8.367105	−9.204235	−2.582439
36	6	0	−9.813384	−7.789026	−3.180779
37	1	0	−10.208415	−6.902217	−2.705235
38	1	0	−10.620399	−8.506802	−3.264757
39	6	0	−9.230673	−7.465732	−4.551371
40	1	0	−8.441445	−6.727179	−4.475776
41	1	0	−10.011160	−7.071369	−5.191099
42	1	0	−8.829173	−8.353865	−5.027596
43	1	0	−8.908471	−6.935015	−0.839770
44	6	0	−7.319064	−8.414092	2.227235
45	1	0	−7.524794	−7.655497	2.975086
46	1	0	−6.495183	−9.025344	2.589524
47	1	0	−8.191742	−9.049081	2.148880
48	1	0	−5.577882	−6.485278	2.826303
49	6	0	−4.035196	−4.580700	4.103812
50	1	0	−4.404379	−3.720588	4.652586
51	1	0	−3.054991	−4.824385	4.499884
52	1	0	−4.692910	−5.409830	4.314338
53	1	0	−2.469628	−2.516856	4.087013
54	6	0	−0.240114	−2.610432	0.963119
55	1	0	0.843224	−2.655515	0.893994
56	1	0	−0.616557	−2.643018	−0.057047
57	1	0	−0.580355	−3.495378	1.479308

Hartree-Fock = −907.0522872 Hartree; Möller-Plesset second-order perturbation = −910.0153506 Hartree. Excited state 1: 2.6467 eV; 468.45 nm;  $f = 0.6170$ . Zero-point correction = 0.546520 (Hartree/particle). Thermal correction to Gibbs free energy = 0.488475.  $i = -453.5584$ .

**TABLE 3 Product**

Center number	Atomic number	Atomic type	Coordinates (Å)		
			X	Y	Z
1	1	0	−0.734494	0.411166	−0.163606
2	6	0	−0.436357	0.223910	0.866609
3	1	0	0.636127	0.029310	0.825283
4	6	0	−1.117833	−1.040343	1.323335
5	6	0	−1.687120	−1.157360	2.560049
6	6	0	−1.520360	−0.066479	3.650135
7	6	0	−0.528879	1.024314	3.200964
8	1	0	0.487588	0.658402	3.328967
9	1	0	−0.633384	1.880299	3.859630
10	6	0	−0.713183	1.431231	1.747620
11	1	0	−1.719565	1.798645	1.572980
12	1	0	−0.036180	2.238275	1.488866
13	6	0	−2.893363	0.567927	3.951168
14	1	0	−2.800562	1.312903	4.735056
15	1	0	−3.608142	−0.176073	4.288739
16	1	0	−3.315545	1.051099	3.077136
17	6	0	−0.958101	−0.672845	4.952913
18	1	0	−0.060103	−1.252269	4.764072
19	1	0	−1.669698	−1.305093	5.471952
20	1	0	−0.698273	0.127810	5.637457
21	6	0	−2.476842	−2.293073	2.953429
22	6	0	−3.260297	−3.098966	2.151777
23	1	0	−3.349059	−2.845785	1.113568
24	6	0	−4.030372	−4.199018	2.580225
25	6	0	−4.869962	−4.802538	1.627070
26	1	0	−4.846432	−4.393860	0.631503
27	6	0	−5.739126	−5.865924	1.854402
28	6	0	−6.540523	−6.407540	0.844613
29	1	0	−6.443022	−5.957409	−0.126673
30	6	0	−7.441106	−7.466399	1.008513
31	6	0	−8.223556	−7.991777	−0.042807
32	1	0	−8.901534	−8.789300	0.206632
33	6	0	−8.204282	−7.588515	−1.363741
34	7	0	−8.968607	−8.099629	−2.315898
35	1	0	−9.598341	−8.832492	−2.062709
36	6	0	−8.934059	−7.722113	−3.723067
37	1	0	−8.337629	−6.822699	−3.806108
38	1	0	−9.941599	−7.468346	−4.032038
39	6	0	−8.367511	−8.828101	−4.607517
40	1	0	−7.346695	−9.064082	−4.328870
41	1	0	−8.377795	−8.513114	−5.645315
42	1	0	−8.960559	−9.733215	−4.528846
43	1	0	−7.543679	−6.809841	−1.695691
44	6	0	−7.607382	−8.098042	2.370913
45	1	0	−7.925787	−7.364410	3.105562
46	1	0	−6.671532	−8.526412	2.718362
47	1	0	−8.344771	−8.888495	2.350911
48	1	0	−5.799864	−6.282658	2.840718
49	6	0	−3.993537	−4.727215	3.991245
50	1	0	−4.911580	−4.480438	4.518304
51	1	0	−3.163710	−4.335854	4.559312
52	1	0	−3.897100	−5.807490	3.989306
53	1	0	−2.538430	−2.465752	4.009104
54	6	0	−1.023609	−2.141697	0.298613
55	1	0	−0.063135	−2.075307	−0.203055
56	1	0	−1.780560	−2.017507	−0.474463
57	1	0	−1.116157	−3.131952	0.718121

Hartree-Fock = −907.085856 Hartree; Möller-Plesset second-order perturbation = −910.0582937 Hartree. Excited state 1: 2.8796 eV, 430.56 nm,  $f = 2.0275$ . Zero-point correction = 0.547581 (Hartree/particle). Thermal correction to Gibbs free energy = 0.488064.

which was used to focus the pump beam in the BBO crystal for NOPA. As for the generation of the pump beam, we have used a BBO crystal whose thickness and cutting angle were 0.4 mm and  $29^\circ$ , respectively, to generate an SH signal with broad enough bandwidth to sufficiently enhance the phase-matching bandwidth. To amplify most of the spectrum width of the seed beam, there was a temporal overlap of the pump pulse over the seed pulse. Therefore, the seed pulse generated from a 1-mm sapphire window was precompressed by using a pair of  $45^\circ$  quartz prisms separated by  $\sim 50$  cm. To improve the temporal overlap between the pump and seed pulses, the pump pulse is also manipulated to stretch its pulse duration up to  $\sim 500$  fs by passage through a 10-cm quartz block in the optical path of the pump pulse. The stretching of the pulse duration also helps to decrease the peak intensity of the pump pulse and avoid damage to the BBO crystal used for NOPA. Because of the long duration of the pump pulse, the sensitivity to the drift of the pump-seed delay was reduced, and the robustness of NOPA output to environmental disturbance was improved.

The spectral width of the output visible pulse is broad enough to generate sub-4-fs ultrashort laser pulses. For the preset analysis of the ultrafast time-resolved spectroscopy, it is necessary to use ultrashort laser pulses, which can resolve the real-time molecular vibration signal. Therefore, we compressed the generated ultrabroadband visible laser pulse using a compressor, which consists of two dielectric ultrabroadband chirped mirrors, a 300 line/mm ruled diffraction grating whose  $-1$  order diffraction was used, and an  $R = -400$  mm spherical mirror with a flexible mirror positioned in the focal plane. A horizontal angle of the grating was used for the crude compression of the pulse width. For the fine-tuning of the pulse compression, we have adjusted the voltages applied to the piezoelectric array behind the flexible mirror, which has a tuning range of 6  $\mu\text{m}$ .

Under the above tuning process of the grating and deformable mirror, it is necessary to monitor the character of the ultrashort pulse as a guideline value of the alignment procedure. One of the most frequently used methods of pulse characterization of ultrashort pulses is the second harmonic generation (SHG) frequency-resolved optical gating (FROG) technique. Then, we have built up a pulse diagnostic setup based on the SHG FROG with a feedback to a personal computer that controls the piezoelectric array behind the flexible mirror. A translation stage (STC-1020X; SIGMA TECH, Saitama, Japan), which has a built-in interferometer and active position stabilization to obtain position accuracy of 10 nm, was used in the FROG apparatus for the wide- and narrow-range delay scans with adequate accuracy. Two identical Cr-coated 0.5-mm-thick quartz beam splitters, which have virtually flat reflectivity in the visible spectral range, were used to balance the dispersion in both beams of the FROG apparatus. Both of the beams are focused into a wedged ultra-thin  $\beta\text{-BaB}_2\text{O}_4$  crystal for broadband SHG and collimated behind it by  $R = -250$  mm spherical mirror. The thickness of the wedge changes across the face of the crystal from 20  $\mu\text{m}$  to 5  $\mu\text{m}$ . With spectral phase information obtained in the SHG FROG measurement, chirp compensation was performed by adjusting the 39 actuators of the flexible mirror lined up in three rows that provide a clear aperture of  $\sim 30 \times 7 \text{ mm}^2$ .

By use of these compressor instruments, the broadband visible laser pulse was compressed enough to resolve the real-time molecular vibration whose frequency is lower than  $3000 \text{ cm}^{-1}$ . The setup of the SHG FROG measurement system is identical to that of the time-resolved pump-probe measurement system, used for the real-time molecular vibration analysis. Therefore, we also used the SHG FROG setup for the measurement of the time-resolved pump-probe signal. The thin beam splitters used for the SHG FROG measurement split the compressed ultrashort visible laser pulse into pump and probe beams.

## APPENDIX B: CALCULATION OF MOLECULAR STRUCTURE OF THE RETINAL CHROMOPHORE

Geometry optimizations were performed with CIS/6-31G\*\*/CIS/6-31\*, and the calculated results are shown in Tables 1–3.

The authors are grateful to the Information Technology Center of the University of Electro-Communications for their support in the calculation of geometry optimization.

This work was supported by ICORP program of Japan Science and Technology Agency (JST) and the grant MOE ATU Program in NCTU. This work was also partly supported by a Grant-in-Aid for Scientific Research of Japan Society for the Promotion of Science (JSPS-GASR-14002003).

## REFERENCES

- Pollard, W. T., C. H. Brito Crus, C. V. Shank, and R. A. Mathies. 1988. Direct observation of the excited-state cis-trans photoisomerization of bacteriorhodopsin: Multilevel line shape theory for femto-second dynamic hole burning and its application. *J. Chem. Phys.* 88:199–208.
- Oesterhelt, D., and W. Stoekenius. 1995. *Methods of Enzymology, Biomembranes, Part A*, Vol. 31. Academic Press, New York.
- Huang, Y., S. -T. Wu, and Y. Zhao. 2004. All-optical switching characteristics in bacteriorhodopsin and its applications in integrated optics. *Opt. Exp.* 12:895–906.
- Shreve, A. P., and R. A. Mathies. 1995. Thermal effects in resonance Raman scattering: analysis of the Raman intensities of rhodopsin and of the time-resolved Raman scattering of bacteriorhodopsin. *J. Phys. Chem.* 99:7285–7299.
- González-Luque, R., M. Garavelli, F. Bernardi, M. Merchan, M. A. Robb, et al. 2000. Computational evidence in favor of a two-state, two-mode model of the retinal chromophore photoisomerization. *Proc. Natl. Acad. Sci. USA* 97:9379–9384.
- Humphrey, W., H. Lu, I. Logonov, H. J. Werner, and K. Schulten. 1998. Three electronic state model of the primary phototransformation of bacteriorhodopsin. *Biophys. J.* 75:1689–1699.
- Schenki, S., F. van Mourik, G. van der Zwan, S. Haacke, and M. Chergui. 2005. Probing the ultrafast charge translocation of photoexcited retinal in bacteriorhodopsin. *Science* 309:917–920.
- Herbst, J., K. Heyne, and R. Diller. 2002. Femtosecond infrared spectroscopy of bacteriorhodopsin chromophore isomerization. *Science* 297:822–825.
- Haran, G., K. Wynne, A. -H. Xie, Q. He, M. Chance, et al. 1996. Excited state dynamics of bacteriorhodopsin revealed by transient stimulated emission spectra. *Chem. Phys. Lett.* 261:389–395.
- Gai, F., K. C. Hasson, J. C. McDonald, and P. A. Anfinsen. 1998. Chemical dynamics in proteins: The photoisomerization of retinal in bacteriorhodopsin. *Science* 279:1886–1891.
- Stuart, J. A., D. L. Mercy, K. J. Wise, and R. R. Birge. 2002. Volumetric optical memory based on bacteriorhodopsin. *Synth. Met.* 127:3–15.
- Song, L., and M. A. El-Sayed. 1998. Primary step in bacteriorhodopsin photosynthesis: bond stretch rather than angle twist of its retinal excited-state structure. *J. Am. Chem. Soc.* 120:8889–8890.
- Du, M., and G. R. Fleming. 1993. Femtosecond time-resolved fluorescence spectroscopy of bacteriorhodopsin: Direct observation of excited state dynamics in the primary step of the proton pump cycle. *Biophys. Chem.* 48:101–111.
- Kahan, A., O. Nahmias, N. Friedman, M. Sheves, and S. Ruhman. 2007. Photoinduced dynamics in bacteriorhodopsin with 7-fs impulsive vibrational spectroscopy. *J. Am. Chem. Soc.* 129:537–546.
- Hou, B. -X., N. Friedman, M. Ottolenghi, M. Sheves, and S. Ruhman. 2003. Comparing photoinduced vibrational coherences in bacteriorhodopsin and in native and locked retinal protonated Schiff bases. *Chem. Phys. Lett.* 381:549–555.
- Terentis, A. C., Y. Zhou, G. H. Atkinson, and L. Ujj. 2003. Picosecond time-resolved coherent anti-Stokes Raman spectroscopy of the artificial bacteriorhodopsin pigment, BR6.11. *J. Phys. Chem. A* 107:10787–10797.
- Olivucci, M., A. Lami, and F. Santoro. 2005. A tiny excited-state barrier can induce a multiexponential decay of the retinal chromophore: A quantum dynamics investigation. *Angew. Chem. Int. Ed.* 44:5118–5121.
- Hayashi, S., E. Tajkhorshid, and K. Schulten. 2003. Molecular dynamics simulation of bacteriorhodopsin's photoisomerization using ab initio forces for the excited chromophore. *Biophys. J.* 85:1440–1449.

19. Chen, X., and V. S. Batista. 2007. The MP/SOFT methodology for simulations of quantum dynamics: Model study of the photoisomerization of the retinyl chromophore in visual rhodopsin. *J. Photochem. Photobiol. A. Chem.* 190:274–282.
20. Weingart, O. 2007. The twisted C11=C12 bond of the rhodopsin chromophore—a photochemical host spot. *J. Am. Chem. Soc.* 129:10618–10619.
21. Rose, T. S., M. J. Rosker, and A. H. Zewail. 1988. Femtosecond real-time observation of wave packet oscillations (resonance) in dissociation reactions. *J. Chem. Phys.* 88:6672–6673.
22. Polanyi, J. C., and A. H. Zewail. 1995. Direct observation of the transition-state. *Acc. Chem. Res.* 28:119–132.
23. Schotte, F., J. Soman, J. S. Olson, M. Wulff, and P. A. Anfinrud. 2004. Picosecond time-resolved x-ray crystallography: probing protein function in real time. *J. Struct. Biol.* 147:235–246.
24. Siwick, B. J., J. R. Dwyer, R. E. Jordan, and R. J. D. Miller. 2003. An atomic-level view of melting using femtosecond electron diffraction. *Science*. 302:1382–1385.
25. Srinivasan, R., J. S. Feenstra, S. T. Park, S. Xu, and A. H. Zewail. 2005. Dark structures in molecular radiationless transitions determined by ultrafast diffraction. *Science*. 307:558–563.
26. Kobayashi, T., T. Saito, and H. Ohtani. 2001. Real-time spectroscopy of transition states in bacteriorhodopsin during retinal isomerization. *Nature*. 414:531–534.
27. McCamant, D. W., P. Kukura, and R. A. Mathies. 2003. Femtosecond broadband stimulated Raman: A new approach for high-performance vibrational spectroscopy. *Appl. Spectrosc.* 57:1317–1323.
28. Schobert, B., J. Cupp-Vickery, V. Hornak, S. O. Smith, and J. K. Lanyi. 2002. Crystallographic structure of the K intermediate of bacteriorhodopsin: Conservation of free energy after photoisomerization of the retinal. *J. Mol. Biol.* 321:715–726.
29. Matsui, Y., K. Sakai, M. Murakami, Y. Shiro, S. Adachi, et al. 2002. Specific damage induced by X-ray radiation and structural changes in the primary photoreaction of bacteriorhodopsin. *J. Mol. Biol.* 324:469–481.
30. Taiji, M., K. Bryl, M. Nakagawa, M. Tsuda, and T. Kobayashi. 1992. Femtosecond studies of primary photoprocesses in octopus rhodopsin. *Photochem. Photobiol.* 56:1003–1011.
31. Dobler, J., W. Zinth, K. Kaiser, and D. Oesterhelt. 1988. Excited-state reaction dynamics of bacteriorhodopsin studied by femtosecond spectroscopy. *Chem. Phys. Lett.* 144:215–220.
32. Logunov, S. L., L. Song, and M. A. Elsayed. 1994. pH-dependence of the rate and quantum yield of the retinal photoisomerization in bacteriorhodopsin. *J. Phys. Chem.* 98:10674–10677.
33. Casadio, R., H. Gutowitz, P. Moverly, M. Taylor, and W. Stoeckenius. 1980. Light-dark adaption of bacteriorhodopsin in triton-treated purple membrane. *Biochim. Biophys. Acta.* 590:13–23.
34. Mowery, P. C., R. H. Lozier, Q. Chae, Y. -W. Tseng, M. Taylor, et al. 1979. Effect of acid pH on the absorption spectra and photoreactions of bacteriorhodopsin. *Biochemistry*. 18:4100–4107.
35. Frisch, M. J., G. W. Trucks, H. B. Schlegel, G. E. Scuseria, M. A. Robb, et al. 2004. Gaussian 03, Revision D.02. Gaussian, Inc, Wallingford, CT.
36. Baltuška, A., and T. Kobayashi. 2002. Adaptive shaping of two-cycle visible pulses using a flexible mirror. *Appl. Phys. B.* 75:427–443.
37. Joffre, M., D. Hulin, A. Migus, A. Antonetti, C. B. A. Laguillaume, et al. 1988. Coherent effects in pump probe spectroscopy of excitons. *Opt. Lett.* 13:276–278.
38. Hasson, K. C., F. Gai, and P. A. Anfinrud. 1996. The photoisomerization of retinal in bacteriorhodopsin: Experimental evidence for a three-state model. *Proc. Natl. Acad. Sci. USA.* 93:15124–15129.
39. Likforman, J. P., M. Joffre, G. Cheriaux, and D. Hulin. 1995. Control of the spectral-oscillation artifact in femtosecond pump-probe spectroscopy. *Opt. Lett.* 20:2006–2008.
40. Reference deleted in proof.
41. Sharkov, A. V., A. V. Pakulev, S. V. Chekalin, and Y. A. Matveet. 1985. Primary events in bacteriorhodopsin probed by subpicosecond spectroscopy. *Biochim. Biophys. Acta.* 808:94–102.
42. Doig, S. J., P. J. Reid, and R. A. Mathies. 1991. Picosecond time-resolved resonance Raman-spectroscopy of bacteriorhodopsin-J, bacteriorhodopsin-K, bacteriorhodopsin-KL intermediates. *J. Phys. Chem.* 95:6372–6379.
43. Bardeen, C. J., Q. Wang, and C. V. Shank. 1998. Femtosecond chirped pulse excitation of vibrational wave packets in LD690 and bacteriorhodopsin. *J. Phys. Chem. A.* 102:2759–2766.
44. Pollard, W. T., S. L. Dexheimer, Q. Wang, L. A. Peteanu, C. V. Shank, et al. 1992. Theory of dynamic absorption-spectroscopy of nonstationary states. 4. Application to 12-fs resonant impulsive Raman-spectroscopy of bacteriorhodopsin. *J. Phys. Chem.* 96:6147–6158.
45. Smith, S. O., M. S. Braiman, A. B. Myers, J. A. Pardo, J. M. L. Courtin, et al. 1987. Vibrational analysis of the all-trans-retinal chromophore in light-adapted bacteriorhodopsin. *J. Am. Chem. Soc.* 109:3108–3125.
46. Eyring, G., B. Curry, A. Broek, J. Lugtenburg, and R. A. Mathies. 1982. Assignment and interpretation of hydrogen out-of-plane vibrations in the resonance Raman spectra of rhodopsin and bathorhodopsin. *Biochemistry*. 21:384–393.
47. Hayashi, S., E. Tajkhorshid, and K. Schulten. 2002. Structural changes during the formation of early intermediates in the bacteriorhodopsin photocycle. *Biophys. J.* 83:1281–1297.
48. Terentis, A. C., L. Ujj, H. Abramczyk, and G. H. Atkinson. 2005. Primary events in the bacteriorhodopsin photocycle: Torsional vibrational dephasing in the first excited electronic state. *Chem. Phys.* 313:51–62.
49. Vrakking, M. J. J., D. M. Villeneuve, and A. Stolow. 1996. Observation of fractional revivals of a molecular wave packet. *Phys. Rev. A.* 54:R37–R40.
50. Baughman, R. H., J. D. Witt, and K. C. Yee. 1974. Raman spectral shifts relevant to electron delocalization in polydiacetylenes. *J. Chem. Phys.* 60:4755–4759.
51. Kumar, A. T. N., F. Rosca, A. Widom, and P. M. Champion. 2001. Investigations of amplitude and phase excitation profiles in femtosecond coherence spectroscopy. *J. Chem. Phys.* 114:701–724.
52. Kano, H., T. Saito, and T. Kobayashi. 2001. Dynamic intensity borrowing in porphyrin J—aggregates revealed by sub-5-fs spectroscopy. *J. Phys. Chem. B.* 105:413–419.